A New Method to Evaluate the In-plane Compression Behavior of Paperboard for the Deep Drawing Process

Alexander Lenske,[a,*] Tobias Müller,[b] Nicole Ludat,[a] Marek Hauptmann,[a,c] and Jens-Peter Majschak [a]

To evaluate the influence of different normal pressures and the fiber orientation on the in-plane compression behavior of paperboard during the deep drawing process, a new method was developed. In addition, the influence of the wrinkle formation on the dynamic coefficient of friction and the bending resistance was examined. To evaluate the eligibility of the in-plane compression testing method, a validation strategy was developed to compare the results from the new alternative tests with the punch force profiles from the deep drawing process within an empirical model.

DOI: 10.15376/biores.17.2.2403-2427

Keywords: In-plane compression; Friction behavior; Bending resistance; Empirical model; Paperboard; Tribocharging; Deep drawing process; 3D-forming

Contact information: a: Fraunhofer Institute for Processing Technology IVV, Heidelbergerstraße 20, 01189 Dresden, Germany; b: Chair of Processing Machines/Processing Technology, Technische Universität Dresden, Bergstrasse 120, 01069 Dresden Germany; c: Chair of packaging machines and packaging technologies, Steinbeis-Hochschule, Ernst-Augustin-Str. 15, 12489 Berlin, Germany;
** Corresponding author: alexander.lenske@ivv-dresden.fraunhofer.de*

INTRODUCTION

Deep drawing of paperboard with rigid tools and immediate compression is characterized by drawing a paperboard blank with a punch into a forming cavity against the resistance induced through a blankholder (Hauptmann and Majschak 2011). During the forming process a compression force develops in-plane within the paperboard blank due to the excess material from the difference between the outer perimeter of the paperboard blank and the inner perimeter of the forming cavity, resulting in inevitable wrinkles (Hauptmann *et al.* 2015; Wallmeier *et al.* 2015; Müller *et al.* 2017). Mark (2002) presented different methods to characterize the in-plane compression behavior of paperboard within substitute tests, but none of them used a defined normal load orthogonal to the plane of the paperboard blank to simulate the characteristic blankholder force from the deep drawing process.

The purpose of this paper is to present a newly developed method to investigate the in-plane compression behavior of paperboard under a defined normal load orthogonal to the plane of the paperboard blank to meet the requirements of the deep drawing process. The in-plane compression behavior of a commercially available paperboard material was determined based on three different normal loads and the fiber direction of the paperboard sample. To evaluate the eligibility of the newly developed method to investigate the in-plane compression behavior as a substitute test for the deep drawing process, a validation strategy was developed. Within the validation strategy four variations of the deep drawing process were presented to isolate the overlapping process forces of the forming process. In addition to that, the respective punch force profiles of the forming process variations were compared to reconstructed punch force profiles from results of the newly developed in-plane compression method as well as results from friction and bending tests.

EXPERIMENTAL

Materials

In the experiments to be described, the commercially available material called Trayforma Natura (Stora Enso, Imatra, Finland) was used, which consists of three layers of virgin-quality fiber, with a grammage of 350 g/m^2, and a thickness of 0.43 mm to 0.45 mm (www.storaenso.com).

Methods

3-D forming equipment and variants of the deep drawing process

All deep drawing tests were conducted with the same tool-setup in a servo-hydraulic press described in Hauptmann and Majschak (2011). The tool-setup consists of a forming cavity, a blankholder, and a punch, as shown in Fig. 1a. The forming cavity, the blankholder, and the punch were made of polished stainless steel (Material No. X5CrNi18-10 or 1.4301 in accordance with the DIN EN 10027-2 (2015) standard). To reduce the friction between the paperboard sample and the tool surfaces, the blankholder and the upper part of the forming cavity were prepared with self-adhesive PTFE-foil (Polytetrafluorethylene glass fabric foil 0.13 AS AD-T, Hightechflon Films and Fabrics, Konstanz, Germany) (Fig. 1a). Preliminary tests showed that the PTFE-foil could not be applied to the area of the infeed radius and the inner contour of the forming cavity with reproducible results. Therefore, it was only applied to the circular ring surface under the blankholder.

Figure 1a shows also the schematic of deep drawing process variant 1. The geometrical data of the tool-setup, as listed in Tab. 1, was taken from Lenske *et al.* (2017), except for the drawing clearance a_{Gap}. By reducing the radius of the drawing punch r_P, the distance a_{Gap} between cavity and punch increased significantly in relation to the thickness of the paperboard material. Because of that, there was no contact between the paperboard material and the inner contour of the forming cavity, preventing any friction in this area.

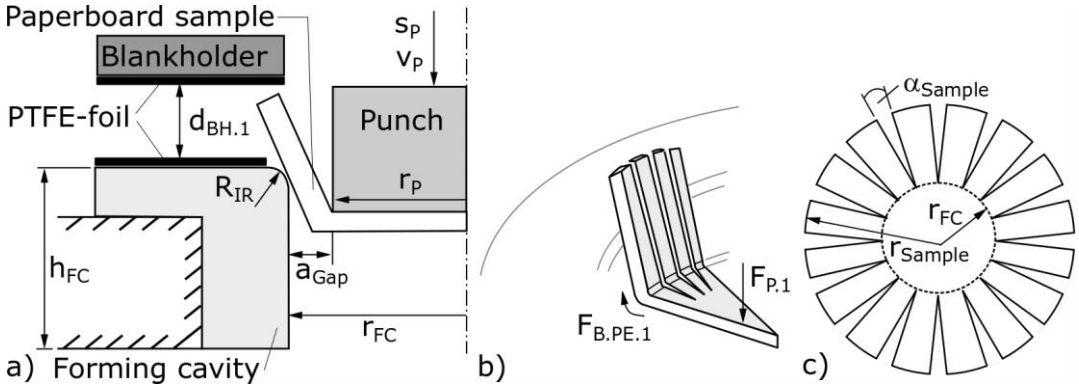

Fig. 1. a) Tool-setup schematic for deep drawing process variant 1 with the location of the self-adhesive PTFE-foil; b) Schematic of the effective process force components during deep drawing process variant 1; c) Schematic of the modified paperboard sample used in deep drawing process variant 1, 2 and 3

The blankholder was positioned at a defined distance $d_{BH.1}$, 30 millimeters above the paperboard sample. Since no blankholder force was applied during deep drawing process variant 1, the friction between the paperboard sample and the tool surfaces could be kept as low as possible, but at the same time the paperboard sample blank was bent around the punch edge. To avoid in-plane compression, the paperboard sample was modified with triangular cutouts (Fig. 1c). Because of that, no excess material was compressed within wrinkles due to the lateral movement of the paperboard material during

the deep drawing process variant. The cutouts were evenly distributed around the circumference of the paperboard sample, each with an opening angle α_{Sample} of 3 ° starting from a radius r_{FC}. These modified paperboard samples were also used in deep drawing process variant 2 and 3. The only effective process force within deep drawing process variant 1 was the bending force around the punch edge $F_{B.PE.1}$ (s_P) (Fig. 1b), which can be measured completely isolated from all other process forces within the punch force $F_{P.1}$ during the punch movement s_P.

Table 1. Geometrical Data and Parameters of the Deep Drawing Process Variants

Radius of the forming cavity r_{FC}	55 mm
Height of the forming cavity h_{FC}	25 mm
Radius of the infeed radius R_{IR}	2 mm
Radius of the punch r_P	53 mm
Drawing clearance a_{Gap}	2 mm
Radius of the paperboard samples r_{Sample}	80 mm
Opening angle of the triangular cutouts α_{Sample}	3 °
Punch movement s_P	50 mm
Paperboard sample movement under the blankholder $s_{PS.BH}$	25 mm
Distance between blankholder and forming cavity $d_{BH.1}$	30 mm
Distance between blankholder and forming cavity $d_{BH.2}$	3 mm
Max. in-plane compression ratio $k_{DDP.4}$	0.31
Constant normal pressure (blank-holder) $p_{N.BH}$	0.3, 0.4, 0.5 MPa
Relative velocity (punch) v_P	20 mm/s

Figure 2a shows the schematic of deep drawing process variant 2. In contrast to deep drawing process variant 1, the blankholder was positioned at a defined distance $d_{BH.2}$, 3 millimeters above the modified paperboard. Since no blankholder force was applied during deep drawing process variant 2, the friction between the modified paperboard sample and the tool surfaces was kept as low as possible, but at the same time the modified paperboard sample blank was bended around the punch edge and the infeed radius. Due to the modified paperboard sample, no in-plane compression occurred. Because of that, the effective process forces within deep drawing process variant 2 were the bending force components around the punch edge $F_{B.PE.2}$ (s_P) and around the infeed radius $F_{B.IR.2}$ (s_P), as well as the spring-back force $F_{B.SB.2}$ (s_P), which could be measured completely isolated from all other process forces within punch force profile $F_{P.2}$ (s_P) (Fig. 2b).

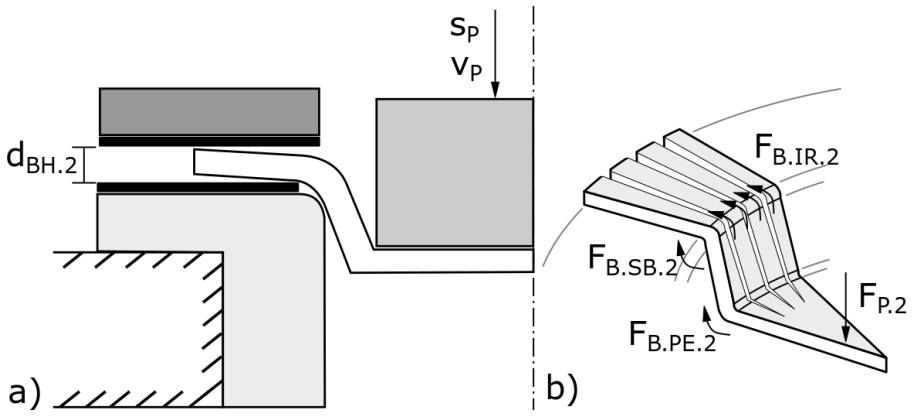

Fig. 2. a) Tool-setup schematic for deep drawing process variant 2 b) Schematic of the effective process force components during deep drawing process variant 2

Figure 3a shows the schematic of deep drawing process variant 3. In contrast to deep drawing process variant 1 and 2, the blankholder applied a constant normal load $p_{N.BH}$ onto the modified paperboard sample. As a result, friction forces were acting between the modified paperboard sample and the blankholder $F_{F.BH.3}$ (s_P), the forming cavity $F_{F.FC.3}$ (s_P), and the infeed radius $F_{F.IR.3}$ (s_P) (Fig. 3a) as an addition to the bending force components $F_{B.PE.3}$ (s_P), $F_{B.IR.3}$ (s_P), and $F_{B.SB.3}$ (s_P) (Fig. 3b). All process forces within deep drawing process variant 3 could be measured within punch force profile $F_{P.3}$ (s_P) (Fig. 3b).

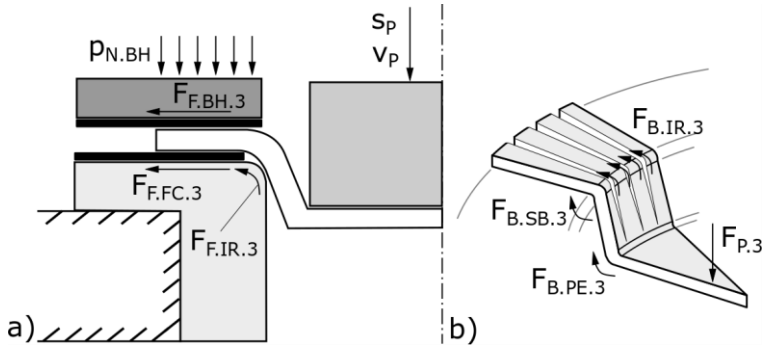

Fig. 3. a) Tool-setup schematic for deep drawing process variant 3 and effective friction force components; b) Schematic of the effective bending force components during deep drawing process variant 3

Figure 4a shows the schematic of deep drawing process variant 4. In contrast to deep drawing process variant 1, 2, and 3, the blankholder applied a constant normal load $p_{N.BH}$ onto a paperboard sample without triangular cutouts (Fig. 4c). As a result, friction forces were active between the paperboard sample and the blankholder $F_{F.BH.4}$ (s_P), the forming cavity $F_{F.FC.4}$ (s_P), and the infeed radius $F_{F.IR.4}$ (s_P) (Fig. 4a) as an addition to the bending force components $F_{B.PE.4}$ (s_P), $F_{B.IR.4}$ (s_P), and $F_{B.SB.4}$ (s_P) and the in-plane compression force $F_{IPC.4}$ (s_P) (Fig. 4b). All process forces within deep drawing process variant 4 could be measured within punch force profile $F_{P.4}$ (s_P) (Fig. 4b).

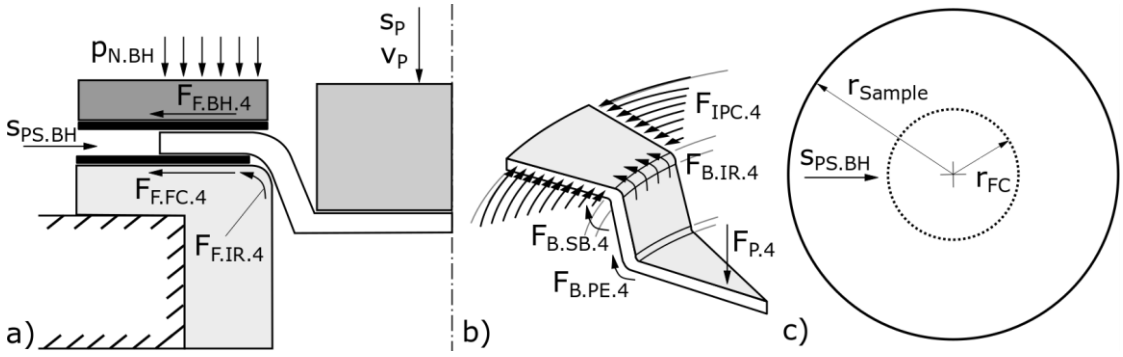

Fig. 4. a) Tool-setup schematic for deep drawing process variant 4 and effective friction force components; b) Schematic of the effective bending and in-plane compression force components during deep drawing process variant 3

To compare the in-plane compression force $F_{IPC.4}$ (s_P) of deep drawing process variant 4 and the results of the newly developed in-plane compression method, the in-plane compression ratio $k_{DDP.4}$ for deep drawing process variant 4 was determined. In general, the in-plane compression ratio k is the ratio between the in-plane compression movement and the total length of the paperboard sample. In deep drawing process variant 4 the maximum in-plane compression movement is the difference between the outer perimeter of the paperboard sample blank and the inner perimeter of the forming cavity (Fig. 4c). The

total length of the paperboard sample is then the outer perimeter of the paperboard sample blank. To describe the progression of the in-plane compression ratio $k_{DDP.4}$, the movement of the paperboard sample below the blankholder $s_{PS.BH}$ was used, which ended after 25 millimeters, when the paperboard sample was completely drawn into the forming cavity (Fig. 4a and 4c).

$$k_{DDP.4}(s_{PS.BH}) = \frac{2\times\pi\times(r_{FC}+s_{PS.BH})-2\times\pi\times r_{FC}}{2\times\pi\times r_{Sample}} \quad (1)$$

In-plane compression measurement equipment

The in-plane compression testing method (Fig. 5a), in the following abbreviated with IPCTM, is based on a similar approach to investigate the in-plane compression behavior of paperboard from Lenske *et al.* (2017a) and mounted on the flexible testing rig described in Lenske *et al.* (2017b).

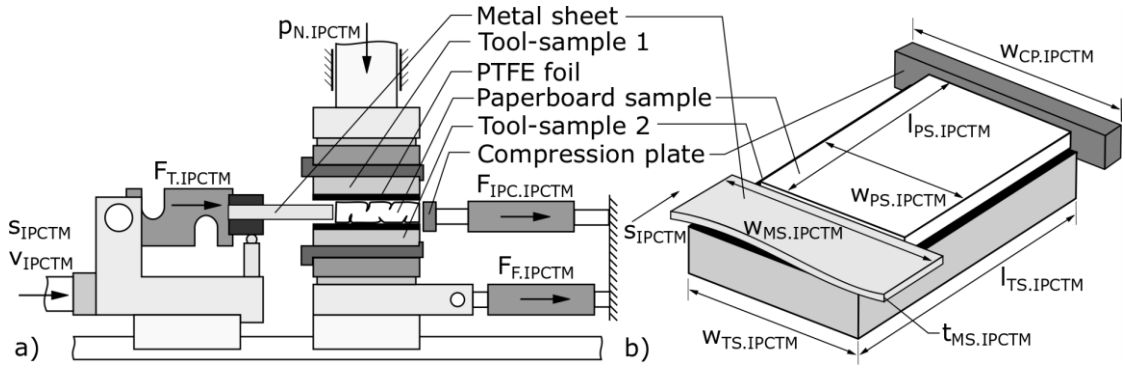

Fig. 5. a) Schematic side-view of the in-plane compression testing method (IPCTM) with tool-samples prepared with PTFE-foil; b) Schematic detail-view of tool-sample 2, the paperboard sample, the compression plate and the metal sheet

A rectangular paperboard sample was positioned between two tool-samples. A compression plate served as end-stop for the paperboard sample. The compression plate was attached to a force sensor (KD9363s, ME Messsysteme, Henningsdorf, Germany; measuring range ± 2,5 kN; accuracy class 0.1%) and the surrounding frame structure. On the other side of the paperboard sample, a metal sheet was attached to a force sensor (KD9363s, ME Messsysteme, Henningsdorf, Germany; measuring range ± 12 kN; accuracy class 0.1%) within a metal frame and could be moved due to the pulling system described in Lenske *et al.* (2017b). The metal sheet must be slightly thinner than the thickness of the paperboard sample to avoid contact between the tool samples and the metal sheet. The thickness of the metal sheet $t_{MS.IPCTM}$ was therefore determined as 0.4 mm (Fig. 5b). During the IPCTM, the upper tool arrangement applied a constant normal pressure $p_{N.IPCTM}$ (s_{IPCTM}) onto the paperboard sample blank due to the force control of the pushing system described in Lenske *et al.* (2017b). The in-plane compression force $F_{IPC.IPCTM}$ resulted from the movement s_{IPCTM} of the metal sheet into the paperboard sample with a defined relative velocity v_{IPCTM} against the end-stop of the compression plate. The compression plate was positioned two tenths of a millimeter from the two tool-samples away, to record the in-plane compression force $F_{IPC.IPCTM}$ (s_{IPCTM}) without disturbance of any other force component such as friction. As a result of the IPCTM, the paperboard samples showed a significant wrinkle formation (Fig. 10). In order to investigate the influence of this wrinkle formation on the friction and bending behavior, the paperboard samples with wrinkle formation were used within the strip-testing method (STM) (Fig. 6a) and the modified two-point bending test (MTPBT) (Fig. 8a). For this purpose, the width of the paperboard samples $w_{PS.IPCTM}$ was expanded (Tab. 2). The paperboard samples with

wrinkle formation for the STM and MTPBT were produced without investigating the in-plane compression force $F_{IPC.IPCTM}$. The tool-samples were fully covered with self-adhesive PTFE foil (Fig. 5a). The in-plane compression ratio was adapted from deep drawing process variant 4 and transferred to the paperboard sample blank for the IPCTM. The geometrical data and parameters used for the IPCTM are listed in Table 2.

$$k_{IPCTM}(s_{IPCTM}) = \frac{s_{IPCTM}}{l_{PS.IPCTM}} \quad (2)$$

Table 2. Geometrical Data and Parameters of the IPCTM

Paperboard sample length $l_{PS.IPCTM}$	42 mm
Paperboard sample width $w_{PS.IPCTM}$	IPCTM: 28 mm STM: 45 mm MTPBT: 95 mm
Max. compression movement s_{IPCTM}	21 mm
Tool sample size $l_{TS.IPCTM}$ x $w_{TS.IPCTM}$	70 mm x 100 mm
Compression plate width $w_{CP.IPCTM}$	100 mm
Metal sheet width $w_{MS.IPCTM}$	100 mm
Metal sheet thickness $t_{MS.IPCTM}$	0.4 mm
Max. In-plane compression ratio k_{IPCTM}	0.5
Constant normal pressure $p_{N.IPCTM}$	0.3 MPa, 0.4 MPa, 0.5 MPa
Relative velocity v_{IPCTM}	20 mm/s

Friction measurement equipment

The evaluation of the friction behavior of the paperboard material was carried out with the strip-testing method (STM) (Fig. 6a), according to Lenske *et al.* (2017b). The tool-samples were fully covered with self-adhesive PTFE foil. The geometry of the tool- and paperboard samples used during the STM are shown in Fig. 6b and listed in Table 3. The orientation of the paperboard sample with wrinkle formation during the STM is shown in Fig. 6c.

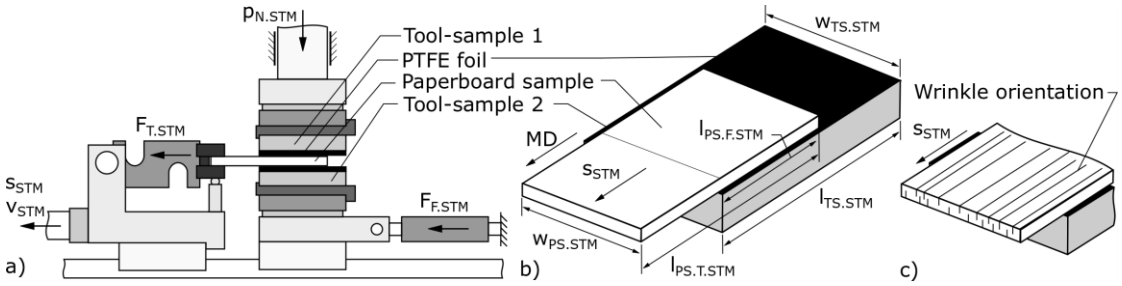

Fig. 6. a) Schematic side-view of the Strip-testing method (STM) according to Lenske *et al.* (2017b) with tool-samples prepared with PTFE-foil; b) Schematic detail-view of tool-sample 2 and a paperboard sample; c) Schematic detail-view of tool-sample 2 and a paperboard sample with wrinkle formation

Table 3. Geometrical Data and Parameters of the STM

Paperboard sample size $l_{PS.T.STM}$ x $w_{PS.STM}$	45 mm x 28 mm
Max. friction length $l_{PS.F.STM}$	28 mm
Sliding movement s_{STM}	28 mm
Tool sample size $l_{TS.STM}$ x $w_{TS.STM}$	70 mm x 32 mm
Constant normal pressure $p_{N.STM}$	0.3 MPa, 0.4 MPa, 0.5 MPa
Relative velocity v_{STM}	20 mm/s

To examine the effect of the transition from the area covered with PTFE-foil into the area consisting of the polished stainless steel within deep drawing process variant 3 and 4 at the infeed radius (Figs. 3a and 4a), the double strip-testing method (DSTM) (Fig. 7a), was used according to Lenske *et al.* (2018). Within the DSTM, the tool-samples were only covered partially with self –adhesive PTFE-foil, representing the area between the blankholder and the upper part of the forming cavity. The length of the PTFE-foil covered area of the tool sample $l_{TS.PTFE.DSTM}$ is shown in Fig. 7b, as well as all other relevant geometry descriptions of the tool and paperboard samples. The infeed radius of the forming cavity was represented through the part of the tool-sample within the DSTM, which was uncovered with PTFE-foil $l_{TS.SS.DSTM}$ and consisted of polished stainless steel (Material No. X5CrNi18-10 or 1.4301 in accordance with the DIN EN 10027-2 (2015) standard). The paperboard sample started the sliding movement s_{DSTM} from the line, which marked the transition from PTFE-foil to polished stainless steel. The geometrical data and parameters used for the DSTM are listed in Table 4. The normal forces, which were used for the DSTM, were selected according to the normal forces in Lenske *et al.* (2018).

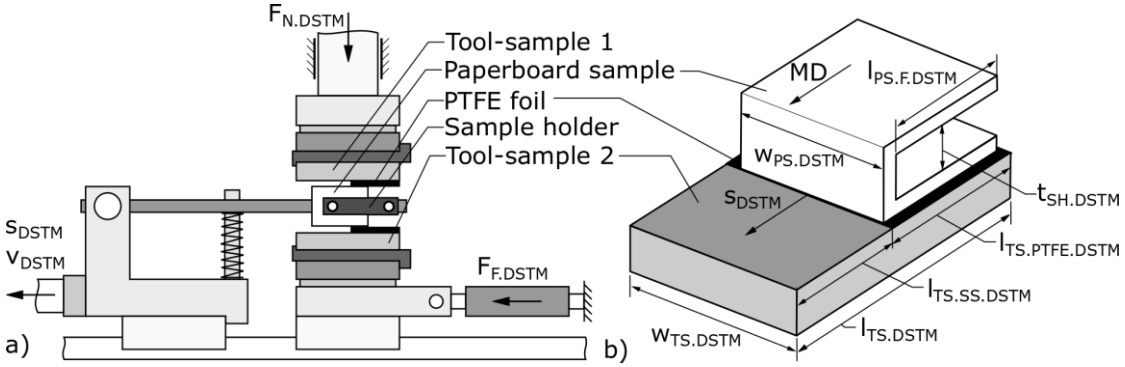

Fig. 7. a) Schematic side-view of the Double strip-testing method (DSTM) according to Lenske *et al.* (2018) with tool-samples partially prepared with PTFE-foil; b) Schematic detail-view of tool-sample 2 and a paperboard sample

Table 4. Geometrical Data and Parameters of the DSTM

Paperboard sample size $l_{PS.F.DSTM}$ x $w_{PS.DSTM}$	25 mm x 28 mm
Sample holder thickness $t_{SH.DSTM}$	14 mm
Tool sample size $l_{TS.STM}$ x $w_{TS.STM}$	70 mm x 32 mm
Length of the PTFE-foil covered area $l_{TS.PTFE.DSTM}$	45 mm
Length of the stainless steel area $l_{TS.SS.DSTM}$	25 mm
Sliding movement s_{DSTM}	50 mm
Constant normal force $F_{N.DSTM}$	400 N, 800 N, 1200 N
Relative velocity v_{DSTM}	20 mm/s

Bending measurement equipment

A modified two-point bending test (MTPBT) (Fig. 8a) according to DIN 53121 (2008) was used to examine the bending resistance of the paperboard material, built on the base of the flexible testing rig from Lenske *et al.* (2017b). For this purpose, the force sensor from the friction measurement system was removed and the lower tool assembly was connected to the machine frame. The upper tool arrangement, driven by an electromechanical servo-cylinder (Serac KH30, Ortlieb, Kirchheim, Germany; constant force range ± 30 kN) could then pass the lower tool arrangement without hindrance. The movement of the upper tool arrangement bent the paperboard sample around the edge of lower tool sample. The bending force $F_{B.MTPBT}$ (s_{MTPBT}) was measured through a force sensor (KD9363s, ME Messsysteme, Hennigsdorf, Germany; measuring range ± 10 kN; accuracy class 0.1%) between the electromechanical servo-cylinder and the upper tool

arrangement and evaluated as bending resistance $W_{B.MTPBT}$ (s_{MTPBT}) in relation to the paperboard sample width $w_{PS.MTPBT}$ in order to compare the results of the MTPBT for paperboard samples without wrinkle formation and paperboard samples with wrinkle formation, which were produced within the IPCTM. Both tool samples were positioned at a defined distance from each other. The distance corresponded to the drawing clearance a_{Gap} within the tool-set of the forming process (Fig. 1a and Table 1). Figure 8b shows the paperboard sample without wrinkle formation and Fig. 8c with wrinkle formation and the corresponding bending lines as an example of the positioning within the MTPBT. Within the deep drawing process, the wrinkles always run radially from the center of the base geometry to the edge of the wall section of the drawn part. Because of that, the bending line is always orthogonal to the direction of the wrinkle orientation. For example, a paperboard sample that was modified during the IPCTM with a wrinkle formation in MD was consequently loaded in the MTPBT orthogonally to the wrinkle orientation, which was arranged parallel to CD. The calculation of the bending resistance $W_{B.MTPBT}$ (s_{MTPBT}) of the paperboard sample with wrinkle formation was also based on the original sample length $l_{PS.IPCTM}$ of 42 mm before the in-plane compression.

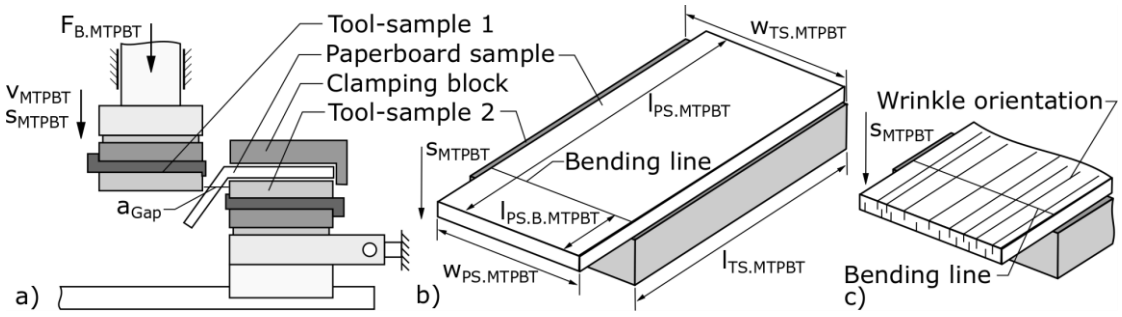

Fig. 8. a) Modified two-point bending test schematic according to DIN 53121 (2008); Positioning of the paperboard sample and the bending line in relation to the fiber-direction during the MTPBT b) without wrinkle formation and c) with wrinkle formation

Table 5 summarizes geometrical data and parameters for the MTPBT.

Table 5. Geometrical Data and Parameters of the MTPBT

Paperboard sample size $l_{PS.MTPBT}$ x $w_{PS.MTPBT}$	95 mm x 28 mm
Paperboard bending length $l_{PS.B.MTPBT}$	25 mm
Tool sample size $l_{TS.MTPBT}$ x $w_{TS.MTPBT}$	70 mm x 32 mm
Tool movement s_{MTPBT}	8 mm
Relative velocity v_{MTPBT}	20 mm/s

Test procedure

To ensure that there was no contamination of the paperboard samples, clean surgical gloves were worn, and the metal tools for the deep drawing process as well as for the substitute tests were cleaned before each test series with a sterile cotton wipe soaked with acetone. In addition to that, before each test series, fresh PTFE-foil was attached to each of the tool surfaces according to the descriptions above. All the repetitions of a test series with the same parameter setup were performed using fresh paperboard samples for each repetition. Each test series performed with the substitute tests and all deep-drawing process variants were performed with 10 repetitions in a row, except for one test series from the STM. To show the influence of triboelectric charging during the friction test, the test series shown in Fig. 13a was performed with 200 repetitions in a row. The tools used for the substitute tests were composed of polished stainless steel (Material No. X5CrNi18-10 or 1.4301 in accordance with the DIN EN 10027-2 (2015) standard) and were separately

grounded on the side of the tool bulk. The deep drawing process variants and the substitute tests were performed under standard climate conditions (23 °C; 50% relative humidity) and with unheated tools at 23 °C.

RESULTS AND DISCUSSION

In-plane Compression

During the IPCTM, the total force $F_{T.IPCTM}$, the in-plane compression force $F_{IPC.IPCTM}$, and the friction force $F_{F.IPCTM}$ against the lower tool sample were recorded according to Figure 5a. Figure 9 shows the progression of the three force curves as a mean value from a test series of 10 repetitions in line of the main fiber direction in MD and with a normal pressure $p_{N.IPCTM}$ of 0.3 MPa. The total force $F_{T.IPCTM}$ must be the sum of the in-plane compression force $F_{IPC.IPCTM}$ and two times the friction force $F_{F.IPCTM}$ from the paperboard sample against both tool samples. Trayforma has the same virgin fiber material layers on both sides. Because of that, the friction force $F_{F.IPCTM}$ should be the same against both tool samples. Figure 9 shows, therefore, the difference $F_{Diff.IPCTM}$ between the total force $F_{T.IPCTM}$ and two times the friction force $F_{F.IPCTM}$. The difference force $F_{Diff.IPCTM}$ and the in-plane compression force $F_{IPC.IPCTM}$ were almost exactly the same in terms of progression and amount, meaning that $F_{IPC.IPCTM}$ was measured without the influence of any friction forces in contrast to the results in Wallmeier *et al.* (2021).

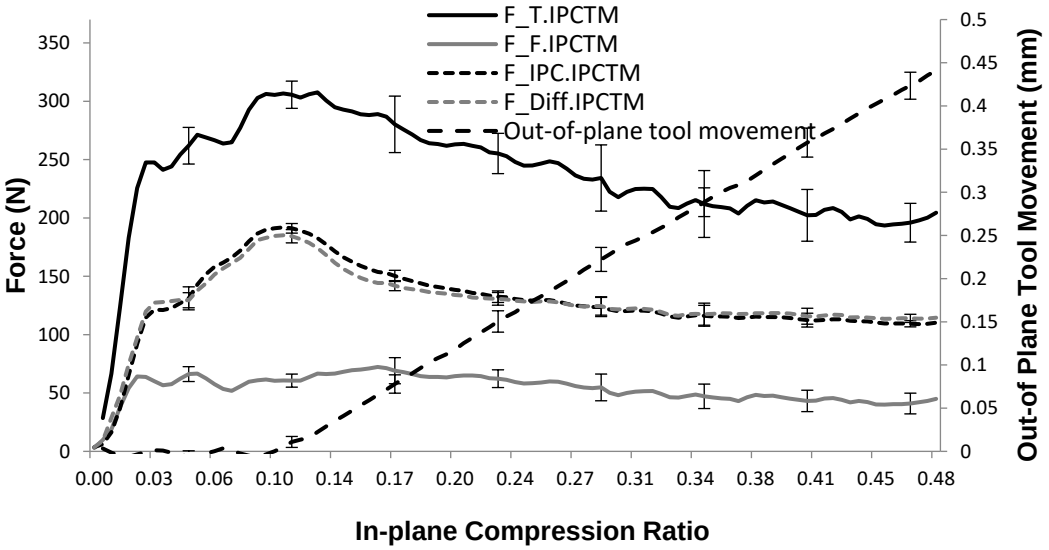

Fig. 9. Measured and calculated force profiles and tool movement during the IPCTM at a normal pressure $p_{N.IPCTM}$ of 0.3 MPa in MD direction of the paperboard sample

The progression of the in-plane compression force $F_{IPC.IPCTM}$ increased steadily at the beginning of the IPCTM to a global maximum and then decreased to an almost constant plateau. The global maximum probably marks the point at which the in-plane compression had exhausted the compensatory capacity of the fiber structure of the paperboard sample mentioned in Hauptmann *et al.* (2015). After this point, the paperboard material must move out of the in-plane to evade the increasing compression force. This assumption is reinforced by evaluating the position of the upper tool sample trough the movement signal of the electromechanical servo-cylinder (Serac KH30, Ortlieb, Kirchheim, Germany; constant force range ± 30 kN). The accumulation of paperboard material results in an increasing counterforce against the normal pressure of the upper tool arrangement. In order to maintain the default constant normal pressure due to the force control of Serac KH30, the

upper tool must move away from the increasing material accumulation. Because of the tool movement, the paperboard material could more easily evade the in-plane compression from the metal sheet, resulting in a reduced compression force $F_{IPC.IPCTM}$ after the global maximum depicted in Fig. 9. To prove this hypothesis, future research should add a camera setup to the IPCTM to record the progression of the wrinkle formation in relation to the position of the metal sheet, similar to the approach described in Wallmeier *et al.* (2021).

Figure 10 shows a paperboard sample from the test series depicted in Fig. 9, after the IPCTM from a side view with a distinct wrinkle formation. The left side of the compressed paperboard sample shows damage of the fiber structure because of the contact with the metal sheet. The metal sheet had penetrated the paperboard sample, slicing the fiber structure apart. In relation to the total length $l_{PS.IPCTM}$ of the paperboard sample the penetration depth must be considered negligible. However, in future work, the penetration depth of the metal sheet and the corresponding thickness of the metal sheet should be observed more closely.

Fig. 10. Paperboard sample after the IPCTM from the test series depicted in Fig. 9, with distinctive wrinkle formation

Figure 11a shows the influence of the anisotropy of the paperboard sample on the progression of the in-plane compression force $F_{IPC.IPCTM}$ for the fiber orientation in MD, CD, and 45° from MD pivoted (MD-45-CD) at 0.3 MPa normal pressure.

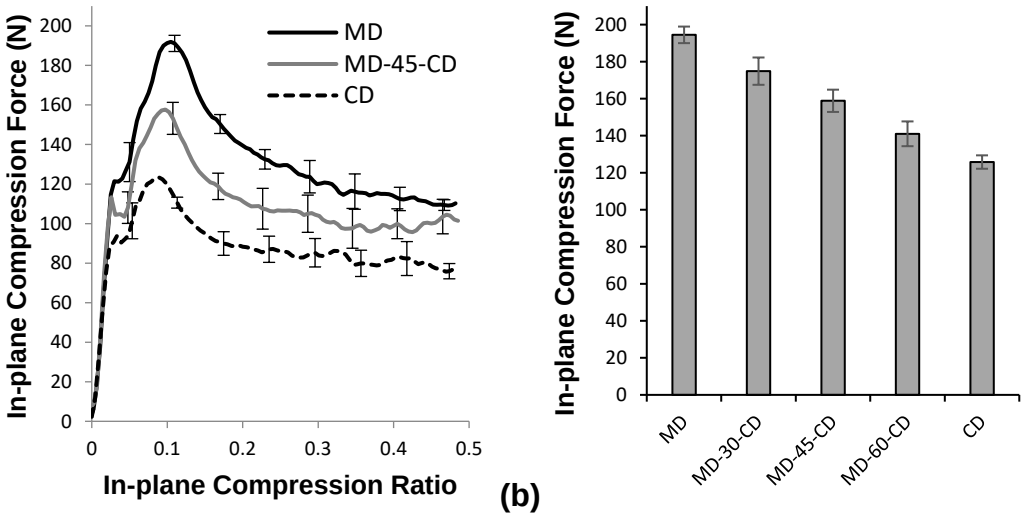

Fig. 11. Influence of the anisotropy of the paperboard sample at a normal pressure $p_{N.IPCTM}$ of 0.3 MPa during the IPCTM on the a) in-plane compression force $F_{IPC.IPCTM}$ (s_{IPCMT}) and b) global maximum values of the in-plane compression force $F_{IPC.IPCTM}$ (s_{IPCMT})

The compression force $F_{IPC.IPCTM}$ was highest along the main fiber orientation in MD. Due to the manufacturing process of natural fiber materials, most of the individual fibers were aligned in MD, compared to only a few in CD. Assuming that the individual fibers act as thin cylinders, the mechanical load along their height can theoretically be viewed as an Euler's buckling case. This means that the individual fiber resisted the external mechanical load until the cylinder structure buckled and finally broke. When the mechanical resistance of the fiber structure was mainly applied by the number of individual

fibers that are arranged along the load direction, the resulting compression force must decrease from MD to CD. The evaluation of the global maxima of the in-plane compression force curves $F_{IPC.IPCTM}$ in Fig. 11b shows a linear relationship between the fiber orientations and the corresponding maximum in-plane compression forces.

The influence of normal pressure on the progression of the in-plane compression force is shown in Fig. 12a for two normal pressures at 0.3 and 0.5 MPa in MD. For a better overview, the normal pressure in between, 0.4 MPa, was omitted. Both in-plane compression force curves were almost identical. This result supported the conceptual model, mentioned above, that the mechanical resistance of the fiber structure was mainly applied only by the number of individual fibers that are arranged along the in-plane load direction. A higher normal pressure orthogonal to the in plane of the paperboard sample decreased only the out-of-plane tool movement and therefore the free spaces where the excess material can go to avoid the in-plane compression force, probably resulting in a better distributed wrinkle formation (Hauptmann and Majschak 2011). Figure 12b shows the global maxima of the in-plane compression force curves for three normal pressure levels in MD, CD, and 45° from MD pivoted (MD-45-CD).

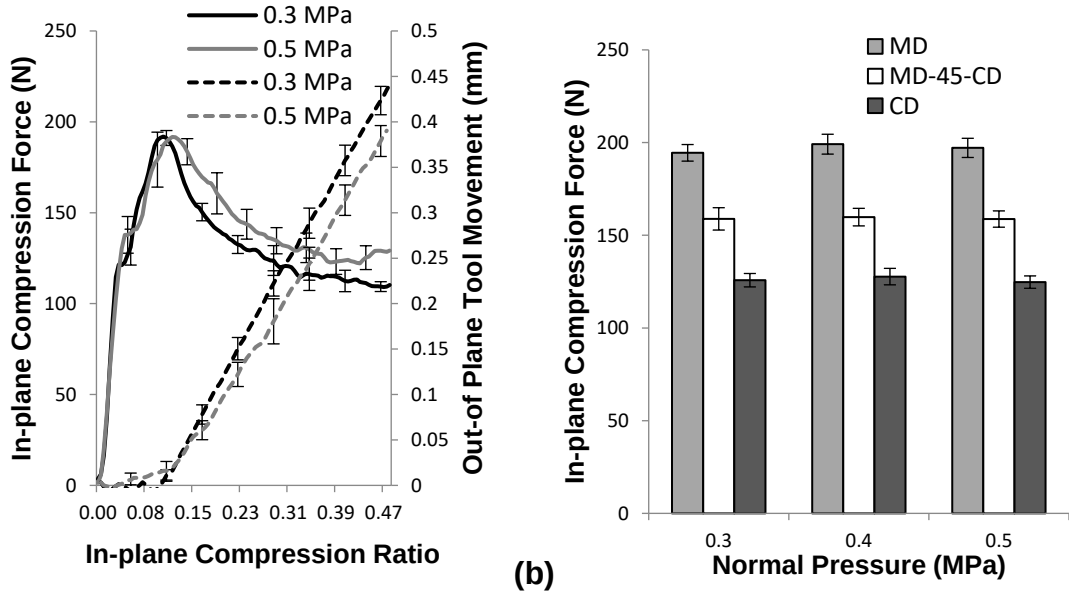

Fig. 12. Influence of the normal pressure $p_{N.IPCTM}$ during the IPCTM on the a) in-plane compression force $F_{IPC.IPCTM}$ (s_{IPCMT}) in MD direction of the paperboard sample and b) global maximum values of the in-plane compression force $F_{IPC.IPCTM}$ (s_{IPCMT}) in MD, MD-45-CD, and CD direction of the paperboard sample

Frictional Behavior

Lenske *et al.* (2017b) showed the influence of the triboelectric charging on the coefficient of friction from paperboard against unheated stainless steel tools. The coefficient of friction increased significantly due to the assumed growth of the triboelectric charging over a high number of repetitions. To examine the influence of the PTFE-foil on the dynamic coefficient of friction in comparison to the results from Lenske *et al.* (2017b), Fig. 13a shows the dynamic coefficient of friction as a mean value from the last 10 tests of two test series with 200 individual repetitions, each performed with the STM at 0.3 MPa normal pressure against PTFE-foil and polished stainless steel. Compared to the dynamic coefficient of friction curve for polished stainless steel, taken from Lenske *et al.* (2017b), the dynamic coefficient of friction against PTFE-foil was significant lower and remained constant over the entire sliding movement. Static and sliding friction are caused by the two main friction mechanisms adhesion and deformation (Bayer and Sirico 1971; Tabor 1981).

Hydrogen bridge bonding is the most common adhesion mechanism between two surfaces in close contact (Tabor 1981). It results from the electrostatic force between a hydrogen atom covalently bonded to a very electronegative atom such as an oxygen atom and another very electronegative atom for instance a second oxygen atom from another water molecule (Jeffrey 1997). PTFE consists of fluoride atoms with high electronegativity, which must cause a high attraction force for hydrogen atoms. But due to this high electronegativity they are on a severe inter molecular bond with their own carbon atoms, meaning that no or only very weak hydrogen bridge bonds can be formed with PTFE (Dunitz and Taylor 1997). On the other hand, triboelectric charging is explained in the literature (Galembeck *et al.* 2014; Zhang *et al.* 2015) primarily with the presence of moisture in the contact area of the friction partners. Diaz and Felix-Navarro (2004) described steel surfaces as hydrophilic, meaning that water can be bonded to the metal surface (Roudgar and Gross 2005). When paperboard is brought into contact with the metal surface, there must be an exchange of charge carriers from the paperboard to the metal surface (Zhang *et al.* 2015), when both surfaces are separated through the friction test. In theory, with the increasing amount of surface water between both contact partners after each repetition of the friction test, more hydrogen bridge bonds can be formed, resulting in an increasing force to separate both surfaces. In addition to that, there must be a saturation effect, when the amount of hydrogen bridge bonds remains constant and therefore the resulting friction force (Fig. 13b). In addition, the coefficient of friction from paperboard against stainless steel remains constantly low, similar to the behavior against PTFE-foil, when the tool surface is heated up to 120 °C (Lenske *et al.* 2017b). Due to the high temperature, the wettability of the metal surface must be reduced. Because of that, the amount of surface water onto the metal is reduced significantly, resulting in a constant coefficient of friction, due to the limited amount of hydrogen bridge bonds. Because of the hydrophobic effect of the PTFE-foil, the number of individual tests for all subsequent test series with PTFE-foil can be limited to 10.

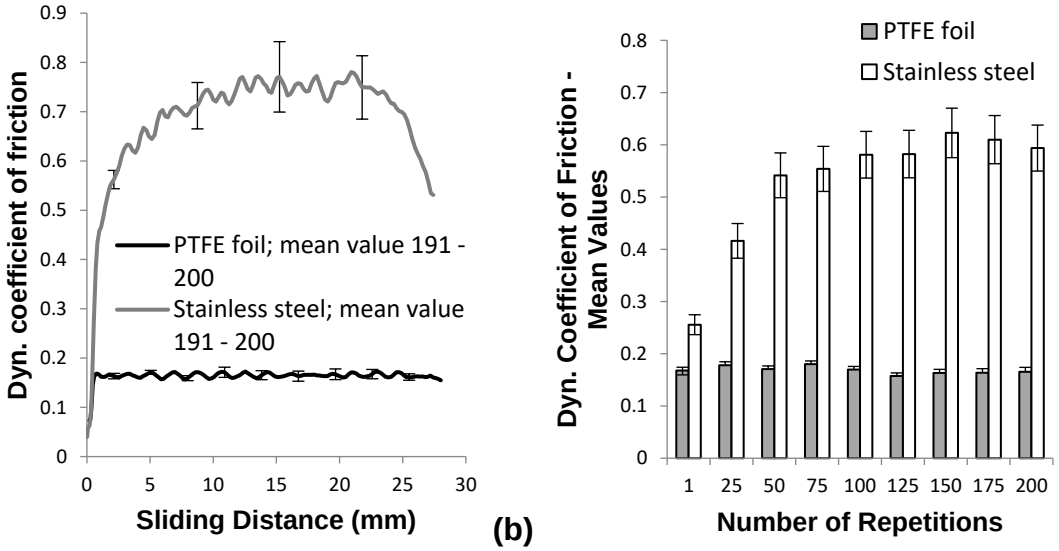

Fig. 13. Influence of the tool-sample surface during the STM at a normal pressure $p_{N.STM}$ of 0.3 MPa on a) the progression of the dynamic coefficient of friction against PTFE-foil and polished stainless steel taken from Lenske *et al.* (2017b) and on b) the progression of the mean values of the dynamic coefficient of friction over 200 repetitions against PTFE-foil and polished stainless steel taken from Lenske *et al.* (2017b)

The influence of the wrinkle formation on the dynamic coefficient of friction can be seen in Fig. 14a as a comparison between the STM performed with paperboard samples with and without wrinkle formation at 0.3 MPa normal pressure in MD. In addition, the dynamic coefficient of friction between the paperboard sample and tool-sample 2 during

the IPCTM was evaluated from the frictional force $F_{F.IPCTM}$ and the constant normal pressure $p_{N.IPCTM}$ in relation to the decreasing paperboard sample surface between both tool samples. The wrinkle formation had no significant influence on the dynamic coefficient of friction, neither longitudinally nor orthogonal to the pulling direction. The same applied to all three normal pressure levels (Fig. 14b). Following the hydrogen bridge bonding theory above, the adhesion force between the paperboard and the PTFE-foil must be limited, due to the hydrophobic effect. Therefore, the friction resistance must be caused mainly by deformation mechanisms. When surface layers came into contact, roughness peaks interlocked with each other, causing contact deformations during a relative motion between both surfaces. The material characteristics of the surface layers, such as shear strength and hardness, as well as normal load, sliding speed, and temperature, had a major influence on the deformation component. The PTFE-foil had a very smooth finish to the surface layer, probably causing the independency between the normal load and the resulting coefficient of friction due to the limited amount of surface interlockings.

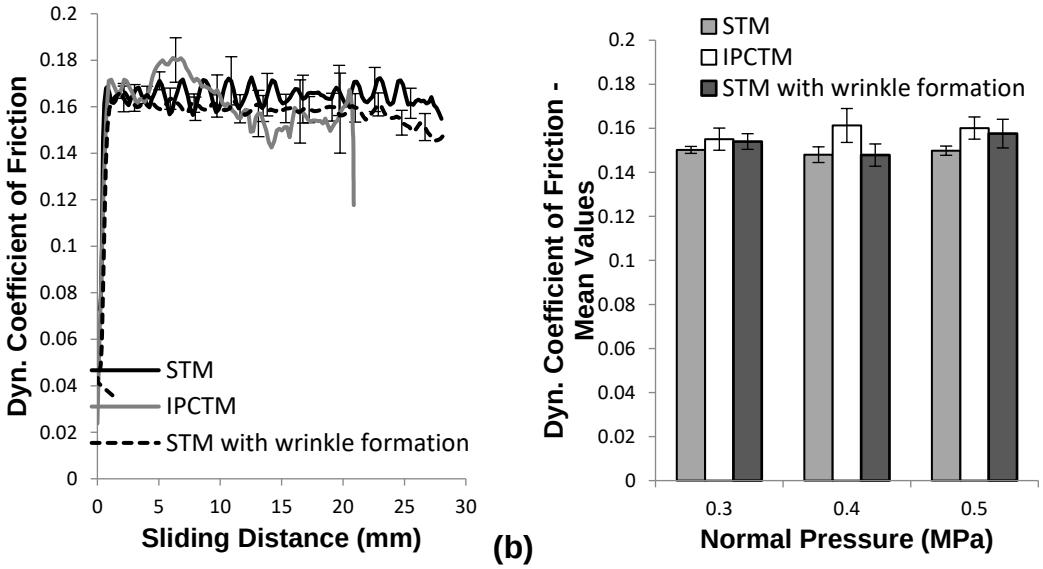

Fig. 14. Influence of the wrinkle formation during the STM and the IPCTM at a normal pressure $p_{N.STM}$ or $p_{N.IPCTM}$ of 0.3 MPa in MD-direction of the paperboard sample on the a) progression of the dynamic coefficient of friction and b) mean value of the dynamic coefficient of friction for three normal pressure levels $p_{N.STM}$ or $p_{N.IPCTM}$

The influence of the transition from PTFE-foil to polished stainless steel on the dynamic coefficient of friction each performed with the DSTM at 400 N or 1200 N constant normal force is shown in Fig. 15a. The dynamic coefficient of friction in the area covered with PTFE-foil up to 25 mm sliding distance was comparable to that in Fig. 13a for tool plates completely prepared with PTFE-foil, supporting the already mentioned normal force independency of the coefficient of friction against PTFE-foil. When the paperboard sample left the area covered with PTFE-foil, the dynamic coefficient of friction decreased significantly, but it remained nearly constant thereafter. In addition to that, the standard deviation showed no growth of the coefficient of friction against polished stainless steel due to triboelectric charging effects mentioned in Lenske *et al.* (2018). In contrast to Lenske *et al.* (2018), the normal force had no influence on the dynamic coefficient of friction after the transition from PTFE-foil to polished stainless steel (Fig. 15b). The normal force dependency of the dynamic coefficient of friction for paperboard against unheated stainless steel tools described in Lenske *et al.* (2018) must be mainly caused by a growing adhesion force component, due to hydrogen bridge bonds. With an increasing normal force, the real area of contact between both surface layers increased likewise (Tabor 1981). With

a higher real contact area, probably more hydrogen bridge bonds could be formed, resulting in a normal force dependency of the coefficient of friction. In addition to that, the transfer of the electrostatic charge must occur immediately when both surfaces come in contact with each other, explaining the transition effect. However, future research should examine the tool surfaces after the friction tests with an electron spectroscopy for chemical analysis, which was used for instance in Gurnagul *et al.* (1992). In addition to controlling the triboelectric charge, the transition effect from PTFE-foil to stainless steel is also of economic importance, especially regarding the production of complex forming cavities inner contours and their preparation with coatings to reduce frictional resistance.

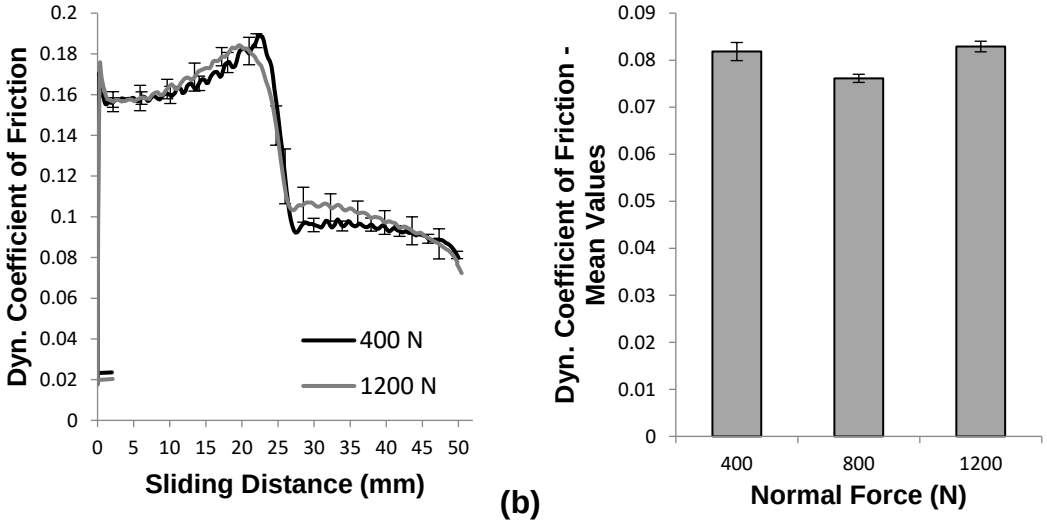

Fig. 15. Influence of the constant normal force $F_{N.DSTM}$ during the DSTM a) on the progression of the dynamic coefficient of friction during the transition from PTFE-foil to polished stainless steel and b) on the mean values of the dynamic coefficient of friction after the transition from PTFE-foil to polished stainless steel

Bending Resistance

Figure 16a shows the influence of the anisotropy of the paperboard sample on the bending resistance $W_{B.MTPBT}$ (s_{MTPBT}) during the MTPBT (Fig. 8b). After 3 to 5 mm of tool movement, the maximum bending resistance was reached and marked the bending break of the paperboard sample. Due to the structural damage, the resulting bending resistance $W_{B.MTPBT}$ (s_{MTPBT}) decreased significantly. In addition, the maximum bending resistance was higher in MD than in CD, probably resulting from the higher number of fibers aligned in MD. Figure 16b shows the influence of the wrinkle formation on the bending resistance during the MTPBT (Fig. 8c). As a result of the additional wrinkle formation, the bending resistance increased significantly in MD and CD, compared to the results from the MTPBT without wrinkle formation (Fig. 16a). The wrinkle formation changed the material cross-section of the paperboard samples for the MTPBT significantly and therefore increased the bending resistance. In addition to that, the bending resistance in MD was smaller than in CD, resulting from the positioning of the paperboard sample with wrinkle formation within the MTPBT (Fig. 8c). The influence of the normal pressure during the IPCTM, when producing the paperboard samples with wrinkle formation for the MTPBT, is shown in Fig. 16c. The normal pressure during the IPCTM had no influence on the bending resistance of the paperboard sample neither in MD nor in CD. The differences between the normal pressure levels were too small to change the cross-section of the paperboard samples significantly, resulting in a similar behavior regarding the bending resistance.

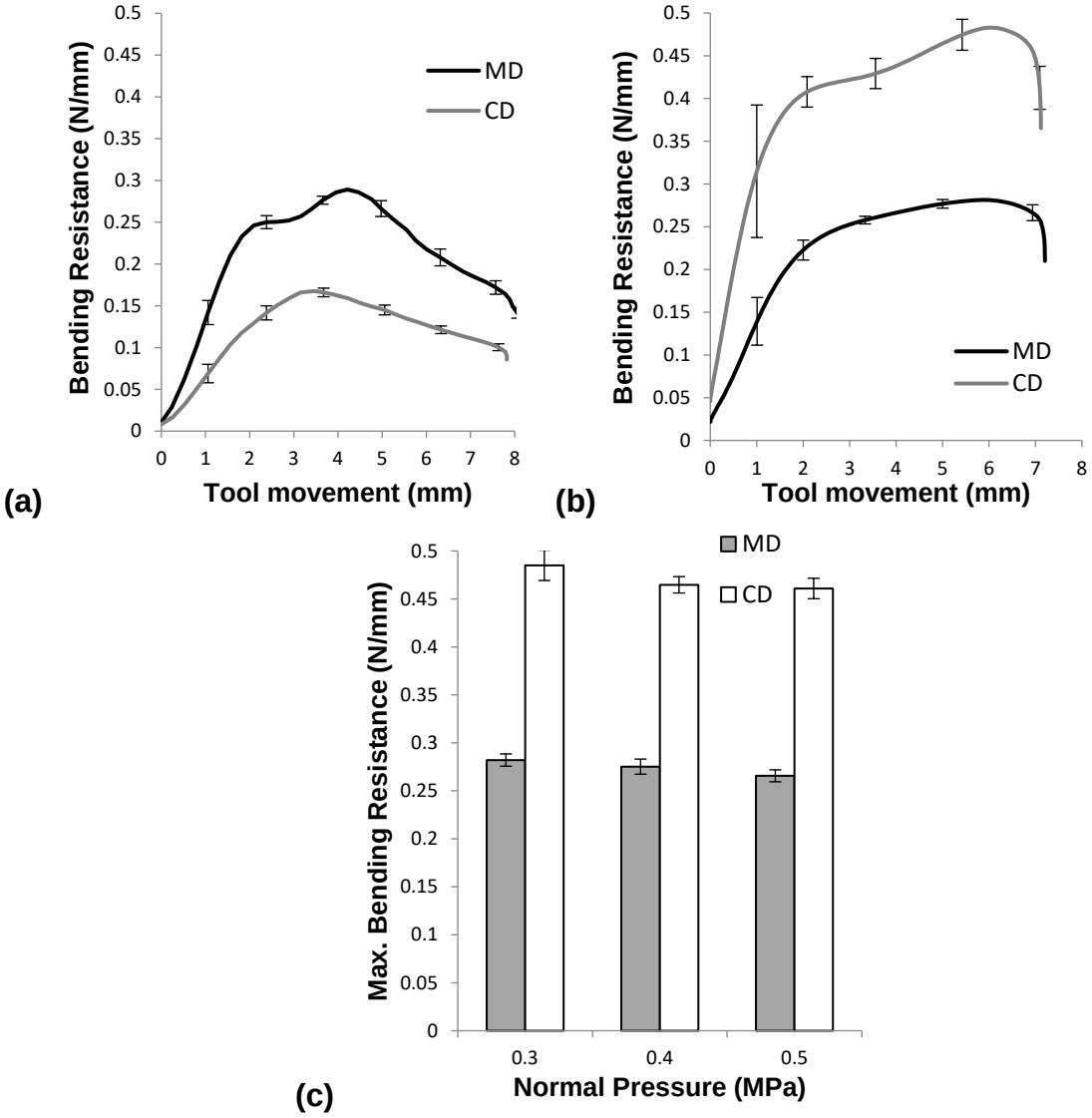

Fig. 16. Progression of the bending resistance $W_{B.MTPBT}$ (s_{MTPBT}) in MD and CD direction of the paperboard sample during the MTPBT a) without wrinkle formation (Fig. 8b) and b) with wrinkle formation (Fig. 8c); c) Influence of the anisotropy of the paperboard sample and the normal pressure $p_{N.IPCTM}$ during the IPCTM on the maximum bending resistance $W_{B.MTPBT}$ (s_{MTPBT}) with wrinkle formation

Validation Strategy and empirical model building

The empirical model for the reconstruction of the punch force profile $F_{P.1}$ (s_P) from deep drawing process variant 1 must represent the bending force around the punch edge $F_{B.PE.1}$ (s_P) as the only effective process force (Fig. 1b). For this purpose, the mean values from the progression of the bending resistance $W_{B.MTPBT}$ (s_{MTPBT}) in MD and CD of the modified two-point bending test are formed and described with a 5-degree polynomial (Fig. 17a). Therefore, the empirical model $F_{PFC.1}$ (s_{MTPBT}) to describe the effective process force components during deep drawing process variant 1 are only valid for tool movement s_{MTPBT}.

$$F_{PFC.1}(s_{MTPBT}) = F_{B.PE.1}(s_{MTPBT}) = 2 \times \pi \times r_P \times W_{B.MTPBT}(s_{MTPBT}) \quad (3)$$

Figure 17b shows the punch force profile $F_{P.1}$ (s_P) from deep drawing process variant 1 and the progression of the empirical model of $F_{PFC.1}$ (s_{MTPBT}) from Eq. 3. The punch force profile $F_{P.1}$ (s_P) showed a steep increase up to a global maximum at about 5

millimeters of punch movement. The global maximum probably marked the bending break at the punch edge, according to the results of the MTPBT (Fig. 16a). After that, the punch force profile decreased immediately. The remaining punch force must be caused from the friction between the modified paperboard sample and the inner contour of the forming cavity. However, the punch force profile and the corresponding empirical model were almost identical, meaning that the results from the modified two-point bending test and the selected modeling approach were sufficiently precise.

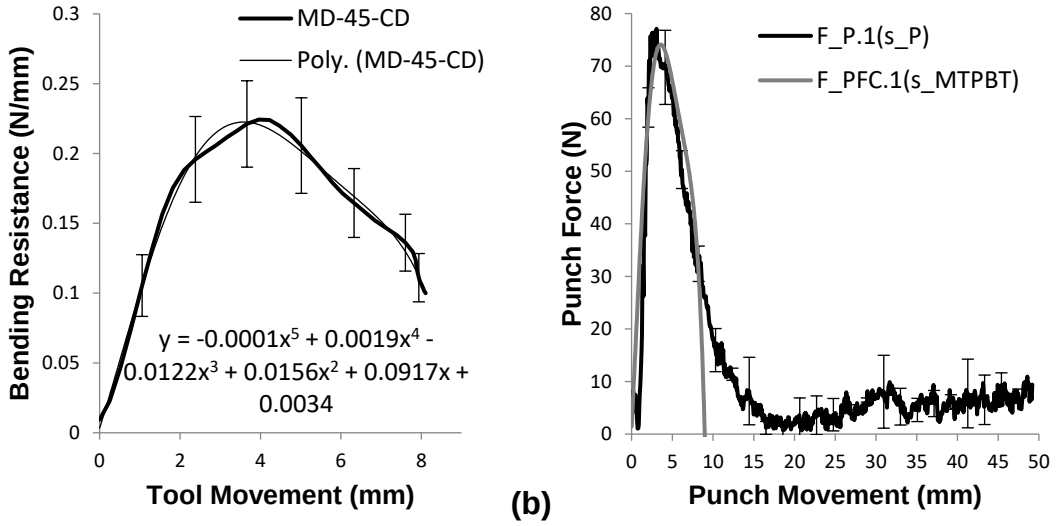

Fig. 17. a) Progression of the bending resistance 45 ° pivoted between MD and CD and corresponding 5th degree polynomial as trendline; b) Comparison between $F_{P.1}$ (s_P) and $F_{PFC.1}$ (s_{MTPBT})

The empirical model for the reconstruction of the punch force profile $F_{P.2}$ (s_P) from deep drawing process variant 2 must represent all active process force components shown in Fig. 2b and was calculated from two partial models. The empirical model is only valid within the movement of the modified paperboard sample below the blankholder $s_{PS.BH}$.

The first partial model described the initial bending break at the two bending lines punch edge and infeed radius of the forming cavity within the first 5 millimeters of paperboard movement $s_{PS.BH}$ according to the results from deep drawing process variant 1 (Fig. 17b) and the MTPBT (Fig. 16a). To calculate the bending force component $F_{B.IR.2}$ ($s_{PS.BH}$), Eq. 4 can be adapted with the geometry of the corresponding bending line around the infeed radius of the forming cavity.

$$F_{B.PE.2}(s_{PS.BH}) = 2 \times \pi \times r_P \times W_{B.MTPBT}(s_{MTPBT}) \quad (4)$$

$$F_{B.IR.2.1}(s_{PS.BH}) = 2 \times \pi \times \left(r_{FC} + \frac{R_{IR}}{2}\right) \times W_{B.MTPBT}(s_{MTPBT}) \quad (5)$$

After that, the bending force $F_{B.PE.2}$ ($s_{PS.BH}$) must decrease completely, according to the results from deep drawing process variant 1 (Fig. 17b). The bending force $F_{B.IR.2}$ ($s_{PS.BH}$), on the other hand, must remain active until the modified paperboard sample has been completely drawn into the forming cavity. As the paperboard movement $s_{PS.BH}$ continues, still unformed material of the modified paperboard sample was bended around the infeed radius, meaning that there was a continued bending break within the material structure. The continued bending break was calculated with the global maximum of the bending resistance curve in Fig. 17a. In addition to that, as the paperboard movement $s_{PS.BH}$ continues, the circumference of the modified paperboard sample increases along the

bending line, which means that the resulting bending force $F_{B.IR.2}$ ($s_{PS.BH}$) must increase at the same time, due to an increase of the material cross-section, until the modified paperboard sample is completely drawn into the forming cavity.

$$F_{B.IR.2.2}(s_{PS.BH}) = 2 \times \pi \times \left(\left(r_{FC} + \frac{R_{IR}}{2}\right) + s_{PS.BH}\right) \times Max.W_{B.MTPBT}(s_{MTPBT}) \quad (6)$$

The spring back force $F_{B.SB.2}$ ($s_{PS.BH}$) must occur when the initial bending break around the infeed radius is complete and remain active as long the bending force $F_{B.IR.2}$ ($s_{PS.BH}$) is active. Through interpolation, the springback force $F_{B.SB.2}$ ($s_{PS.BH}$) was assumed to be 50% of the bending force around the infeed radius of the forming cavity $F_{B.IR.2.2}$ ($s_{PS.BH}$).

$$F_{B.SB.2}(s_{PS.BH}) = 0.5 \times 2 \times \pi \times \left(\left(r_{FC} + \frac{R_{IR}}{2}\right) + s_{PS.BH}\right) \times Max.W_{B.MTPBT}(s_{MTPBT}) \quad (7)$$

The empirical model for the process force components $F_{PFC.2}$ ($s_{PS.BH}$), which were active during deep drawing process variant 2, was calculated from Eq. 8 and compared to the punch force profile $F_{P.2}$ (s_P) (Fig. 18). Within Eq. 8, Eqs. 4 and 5 are valid for the paperboard movement $s_{PS.BH}$ from 0 to 5 millimeters and Eqs. 6 and 7 are valid for the paperboard movement $s_{PS.BH}$ from 5 to 25 millimeters.

$$F_{PFC.2}(s_{PS.BH}) = F_{B.PE.2}(s_{PS.BH}) + F_{B.IR.2.1}(s_{PS.BH}) + F_{B.IR.2.2}(s_{PS.BH}) + F_{B.SB.2}(s_{PS.BH}) \quad (8)$$

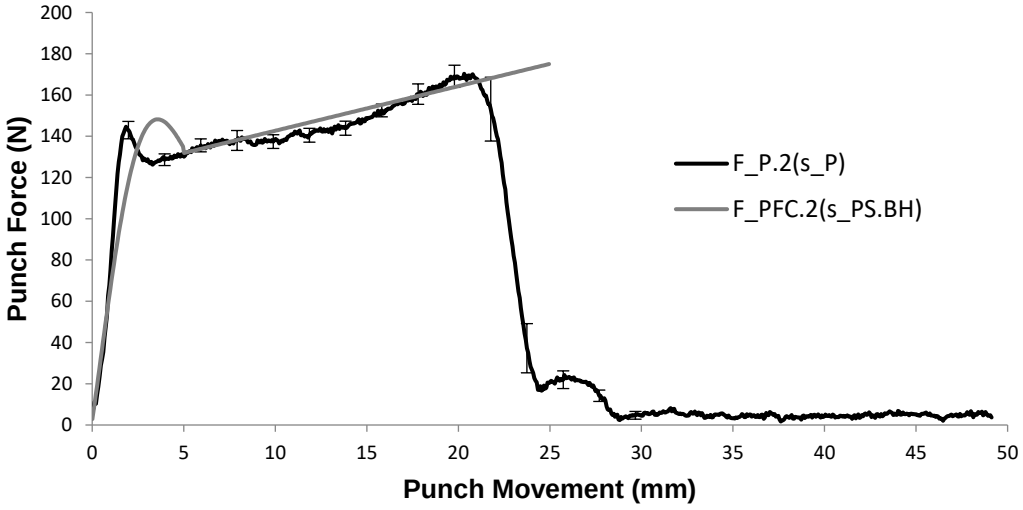

Fig. 18. Comparison between punch force profile $F_{P.2}$ (s_P) and the empirical model of the process force components $F_{PFC.2}$ ($s_{PS.BH}$) during deep drawing process variant 2

The punch force profile $F_{P.2}$ (s_P) shows a steep increase up to a local maximum at approx. 4 millimeters of punch movement. This presumably marks the initial bending break at the two bending lines. The punch force profile $F_{P.2}$ (s_P) then drops slightly and rises again to a global maximum. The paperboard sample is exposed to a constant bending load at the infeed radius of the forming cavity, which only ends when the material is completely drawn into the forming cavity. As the punch movement continues, the circumference of the formed material increases along the bending line, which means that the resulting punch force must increase at the same time, due to an increase of the material cross-section. As soon as the paperboard sample leaves the area below the blankholder after approx. 25 millimeters, the punch force profile decreases almost completely. The punch force profile $F_{P.2}$ (s_P) and the sum of all process force components $F_{PFC.2}$ ($s_{PS.BH}$) from Eq. 8 are almost identical, meaning that the modeling approach must be sufficient.

The empirical model for the reconstruction of the punch force profile $F_{P.3}$ (s_P) from deep drawing process variant 3 must represent all bending force components shown in Fig. 3b, in addition to all friction force components shown in Fig. 3a. The empirical model is only valid within the movement of the modified paperboard sample below the blankholder $s_{PS.BH}$. To calculate the bending force components, Eq. 8 was used, according to the results shown in Fig. 18. To reconstruct the frictional forces between the modified paperboard sample and the blankholder $F_{F.BH.3}$ (s_P) or the forming cavity $F_{F.FC.3}$ (s_P), a logarithmic trendline (Fig. 19a) was derived from the results of the STM from Figure 13a. According to Amontons (1699), the friction force results from the product of the coefficient of friction μ and the normal pressure p_N in relation to a defined area A. The effective area below the blankholder corresponds to a circular ring, which decreased with increasing punch movement until the modified paperboard sample was completely drawn into the forming cavity after 25 mm.

$$F_{F.BH.3}(s_{PS.BH}) = \mu_{STM}(s_{STM}) \times p_{N.BH} \times \pi \times \left(\left(r_{Sample} - s_{PS.BH}\right)^2 - (r_{FC} + R_{IR})^2\right) \quad (9)$$

$$F_{F.FC.3}(s_{PS.BH}) = \mu_{STM}(s_{STM}) \times p_{N.BH} \times \pi \times \left(\left(r_{Sample} - s_{PS.BH}\right)^2 - (r_{FC} + R_{IR})^2\right) \quad (10)$$

The capstan equation or the Euler-Eytelwein formula was used to calculate the friction force around the infeed radius $F_{F.IR.3}$ (s_P) according to Hauptmann (2010). The coefficient of friction in the area of the infeed radius was calculated from a 2nd degree polynomial as a trendline (Fig. 19a) from the results during the DSTM at 800 N constant normal force after the transition from PTFE-foil to polished stainless steel. The holding force $F_{Holding.3}$ ($s_{PS.BH}$) was calculated from the summation of the friction force components $F_{F.BH.3}$ ($s_{PS.BH}$) and $F_{F.FC.3}$ ($s_{PS.BH}$) in Eq. 12.

$$F_{F.IR.3}(s_{PS.BH}) = \left(e^{\mu_{DSTM}(s_{DSTM}) \times arctan\left(\frac{s_{PS.BH}}{a_{Gap}}\right)} - 1\right) \times F_{Holding.3}(s_{PS.BH}) \quad (11)$$

$$F_{Holding.3}(s_{PS.BH}) = F_{F.BH.3}(s_{PS.BH}) + F_{F.FC.3}(s_{PS.BH}) \quad (12)$$

The empirical model for all process force components $F_{PFC.3}$ ($s_{PS.BH}$), which were active during deep drawing process variant 3, was calculated from Eq. 13, as summation of Eqs. 8 through 11.

$$F_{PFC.3}(s_{PS.BH}) = F_{PFC.2}(s_{PS.BH}) + F_{F.BH.3}(s_{PS.BH}) + F_{F.FC.3}(s_{PS.BH}) + F_{F.IR.3}(s_{PS.BH}) \quad (13)$$

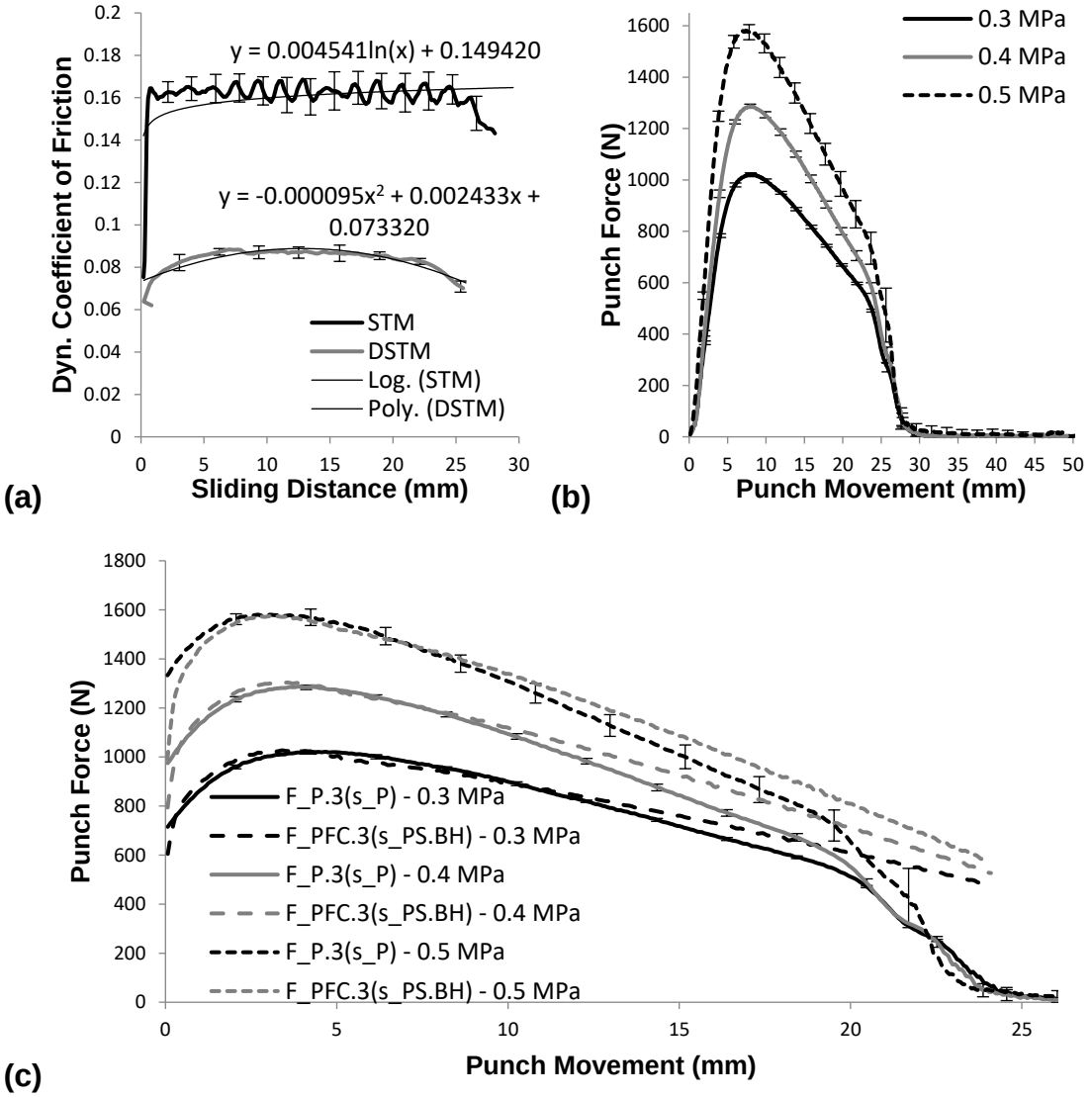

Fig. 19. a) Progression of the dynamic coefficients of friction from the STM and the DSTM for 0.3 MPa or 800 N and the associated trendlines; b) Punch force profiles $F_{P.3}$ (s_P) from forming process variant 3 for three blank holder pressure levels; c) Comparison between punch force profile $F_{P.3}$ (s_P) and the empirical model of all active process force components $F_{PFC.3}$ ($s_{PS.BH}$) during forming process variant 3 for three blankholder pressure levels

Figure 19b shows the punch force profile $F_{P.3}$ (s_P) during deep drawing process variant 3 at three different normal pressures from the blankholder. The punch force curve increased to a global maximum at approximately 4 to 5 millimeters of punch movement. After that, the punch force profile decreased steadily until the modified paperboard sample was completely drawn into the forming cavity. It is noteworthy that the punch force profile decreased completely after a punch movement of approximately 28 mm, but the estimated drawing height must be 25 mm due to the modified paperboard sample geometry (Tab. 1). Hauptmann (2010) described an expansion of the paperboard sample under the normal load of the blankholder, whereby the sample blank was presumably held longer under the blankholder. The occurring strain effect was only taken into account indirectly within the empirical model, while the punch force curve was viewed retrospectively 25 millimeters from the position at which the punch force had completely decreased. After that, the adjusted punch force profile $F_{P.3}$ (s_P) was compared to the empirical model for all active process force components $F_{PFC.3}$ ($s_{PS.BH}$) during deep drawing process variant 3 at three different normal pressures from the blankholder (Fig. 19c). The empirical model curves

were almost exactly the same as the measured punch force profiles for all three examined blankholder pressures. This means, that the assumptions from the substitute tests and the modelling approach seem to be correct.

The empirical model for the reconstruction of the punch force profile $F_{P.4}$ (s_P) from deep drawing process variant 4 must represent all active force components shown in Figs. 4a and 4b. To reconstruct the in-plane compression force $F_{IPC.4}$ (s_P) with results from the IPCTM, the in-plane compression force $F_{IPC.IPCTM}$ (s_{IPCTM}) must be transferred from the IPCTM related paperboard sample (Fig. 5b) to the area of the paperboard sample, which was under in-plane compression during deep drawing process variant 4 (Fig. 4c). For this purpose, the in-plane compression force $F_{IPC.IPCTM}$ (s_{IPCTM}) was related to the decreasing surface of the paperboard sample $A_{PS.IPCTM}$ (s_{IPCTM}) and referred to as in-plane compression resistance $W_{IPC.IPCTM}$ (s_{IPCTM}).

$$W_{IPC.IPCTM}(s_{IPCTM}) = \frac{F_{IPC.IPCTM}(s_{IPCTM})}{w_{PS.IPCTM} \times (l_{PS.IPCTM} - s_{IPCTM})} \quad (14)$$

A trendline was derived from the in-plane compression resistance $W_{IPC.IPCTM}$ (s_{IPCTM}) relative to the in-plane compression ratio k_{IPCTM} (s_{IPCTM}) using a polynomial of the 6th degree (Fig. 20a). After that, the in-plane compression resistance $W_{IPC.IPCTM}$ (k_{IPCTM}) was transferred to the paperboard sample blank surface, which was under in-plane compression during deep drawing process variant 4.

$$F_{IPC.4}(s_{PS.BH}) = \pi \cdot \left(\left(r_{Sample} - s_{PS.BH} \right)^2 - (r_{FC})^2 \right) \times W_{IPC.IPCTM}(k_{DDP}) \quad (15)$$

The in-plane compression force $F_{IPC.4}$ ($s_{PS.BH}$) is aligned radially to the circumference of the paperboard sample (Fig. 4b). To calculate the in-plane compression force component $F_{IPC.PFC.4}$ ($s_{PS.BH}$) of the punch force profile $F_{P.4}$ (s_P) during deep drawing process variant 4, $F_{IPC.4}$ ($s_{PS.BH}$) must be aligned in the direction of the punch movement s_P, using a trigonometric tangent function.

$$F_{IPC.PFC.4}(s_{PS.BH}) = \frac{F_{IPC.4}(s_{PS.BH})}{tan^{-1}\left(\frac{(2 \times \pi \times r_{Sample}) - (2 \times \pi \times r_{FC})}{r_{Sample} - r_{FC}} \right)} \quad (16)$$

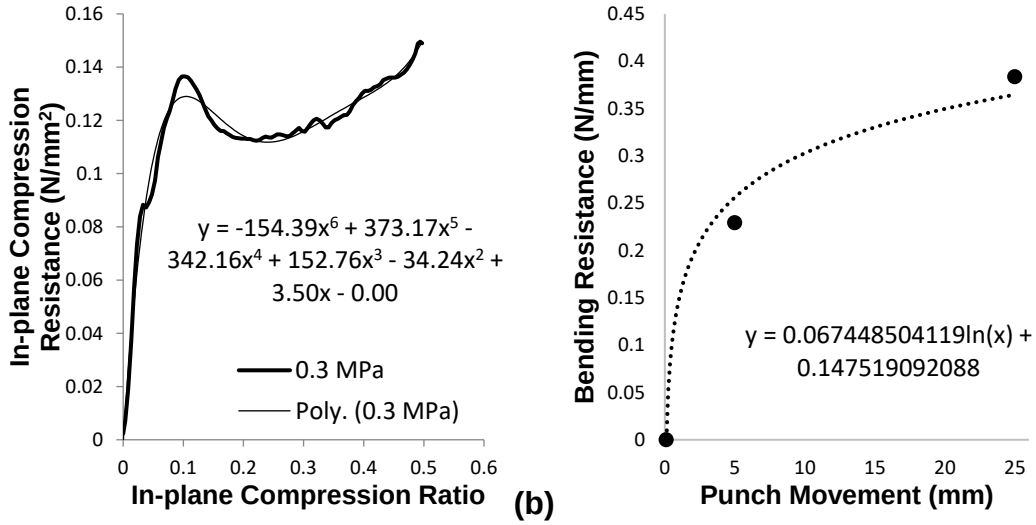

Fig. 20. a) Progression of the in-plane compression resistance $W_{IPC.IPCTM}$ (k_{IPCTM}) from the IPCTM at 0.3 MPa and the associated trendline; b) Interpolated progression curve of the bending resistance $W_{B.4}$ ($s_{PS.BH}$) with increasing wrinkle formation

To calculate the bending force components $F_{B.PFC.4}$ ($s_{PS.BH}$), which are active during deep drawing process variant 4 (Fig. 4b), the influence of the wrinkle formation on the bending resistance $W_{B.MTPBT}$ (s_{MTPBT}) (Fig. 16b and 16c) must be considered within the empirical model building. Hauptmann *et al.* (2015) and Müller *et al.* (2017) showed that no wrinkles occur during the first couples of millimeters of punch movement during the deep drawing process with immediate compression, because the excess material is compressed within the material structure. Accordingly, the initial bending break around the punch edge $F_{B.PE.4}$ (s_P) can be calculated with Eq. 4 until 5 millimeters of punch movement. After that, it was assumed that wrinkles were forming until the paperboard sample was completely drawn into the forming cavity. Accordingly, the bending resistance around the infeed radius $F_{B.IR.4}$ (s_P) and the springback force $F_{B.SB.4}$ (s_P) must be increasing due to the increasing material accumulation within the wrinkle formation. To calculate both bending force components, an increasing bending resistance profile $W_{B.4}$ ($s_{PS.BH}$) was interpolated from three known bending resistances. There was no bending resistance before the punch movement started. According to the results from deep drawing process variant 1 (Fig. 17b) and deep drawing process variant 2 (Fig. 18), the initial bending break was reached after approximately 5 millimeter of punch movement, with no wrinkle formation yet. After a punch movement of 25 millimeter, the material accumulation of the wrinkle formation must result in a global maximum of the bending resistance, which can be taken from Figs. 16b and 16c. The resulting trendline of the interpolated bending resistance profile $W_{B.4}$ ($s_{PS.BH}$) in relation to the movement of the paperboard sample under the blankholder $s_{PS.BH}$ (Fig. 20b) can be used to calculate the bending force components $F_{B.IR.4}$ ($s_{PS.BH}$) and $F_{B.SB.4}$ ($s_{PS.BH}$) with Eqs. 17 and 18.

$$F_{B.IR.4}(s_{PS.BH}) = 2 \times \pi \times \left(\left(r_{FC} + \frac{R_{IR}}{2}\right) + s_{PS.BH}\right) \times W_{B.4}(s_{PS.BH}) \quad (17)$$

$$F_{B.SB.4}(s_{PS.BH}) = 0.5 \times 2 \times \pi \times \left(\left(r_{FC} + \frac{R_{IR}}{2}\right) + s_{PS.BH}\right) \times W_{B.4}(s_{PS.BH}) \quad (18)$$

The empirical model for all bending force components $F_{B.PFC.4}$ ($s_{PS.BH}$), which were active during deep drawing process variant 4, was calculated as summation from Eqs. 4, 17, and 18. Within Eq. 19, Eq. 4 is only valid for the paperboard movement $s_{PS.BH}$ from 0 to 5 millimeters and Eqs. 17 and 18 are valid for the paperboard movement $s_{PS.BH}$ from 0 to 25 millimeters.

$$F_{B.PFC.4}(s_{PS.BH}) = F_{B.PE.2}(s_{PS.BH}) + F_{B.IR.4}(s_{PS.BH}) + F_{B.SB.4}(s_{PS.BH}) \quad (19)$$

To reconstruct the friction force components $F_{F.BH.4}$ (s_P) and $F_{F.FC.4}$ (s_P), Eqs. 9 and 10 were used in combination with the results from the STM (Fig. 19a). To calculate the friction force around the infeed radius $F_{F.IR.4}$ (s_P), Eq. 20 was used. In contrast to deep drawing process variant 3, the in-plane compression force component $F_{IPC.PFC.4}$ ($s_{PS.BH}$) must be implemented when calculating the holding force $F_{Holding.4}$ ($s_{PS.BH}$) in Eq. 21.

$$F_{F.IR.4}(s_{PS.BH}) = \left(e^{\mu_{DSTM}(s_{DSTM}) \times arctan\left(\frac{s_{PS.BH}}{a_{Gap}}\right)} - 1\right) \times F_{Holding.4}(s_{PS.BH}) \quad (20)$$

$$F_{Holding.4}(s_{PS.BH}) = F_{F.BH.3}(s_{PS.BH}) + F_{F.FC.3}(s_{PS.BH}) + F_{IPC.PFC.4}(s_{PS.BH}) \quad (21)$$

The empirical model for all friction force components $F_{F.PFC.4}$ ($s_{PS.BH}$), which were active during deep drawing process variant 4, was calculated as summation from Eqs. 9, 10, and 20.

$$F_{F.PFC.4}(s_{PS.BH}) = F_{F.BH.3}(s_{PS.BH}) + F_{F.FC.3}(s_{PS.BH}) + F_{F.IR.4}(s_{PS.BH}) \quad (22)$$

The empirical model for all process force components $F_{PFC.4}$ ($s_{PS.BH}$), which were active during deep drawing process variant 4, was calculated from Eqs. 16, 19, and 22.

$$F_{PFC.4}(s_{PS.BH}) = F_{IPC.PFC.4}(s_{PS.BH}) + F_{B.PFC.4}(s_{PS.BH}) + F_{F.PFC.4}(s_{PS.BH}) \quad (23)$$

Figure 21 shows the comparison between the punch force profile $F_{P.4}$ (s_P) and the empirical model of all process force components $F_{PFC.4}$ ($s_{PS.BH}$), which were active during deep drawing process variant 4, at three different normal pressures from the blankholder. Similar to the results from deep drawing process variant 3 (Fig. 19b), the punch force profile $F_{P.4}$ (s_P) decreased completely after a punch movement of approximately 28 mm, due to the supposed elongation effect. Because of that, the punch force profile $F_{P.4}$ (s_P) was viewed retrospectively 25 mm from the position at which the punch force had completely decreased, according to the results in Fig. 19c. Similar to the punch force profile $F_{P.3}$ (s_P) during deep drawing process variant 3, the punch force profile $F_{P.4}$ (s_P) increased to a global maximum at approximately 5 to 7 mm of punch movement. The punch force curve then decreased steadily until the sample blank was completely drawn into the forming cavity.

The empirical model curves were almost exactly the same as the measured punch force profiles for all three examined blankholder pressures. Because of that, the results from the newly developed method to investigate the in-plane compression behavior of paperboard IPCTM can be used as a substitute test for the deep drawing process.

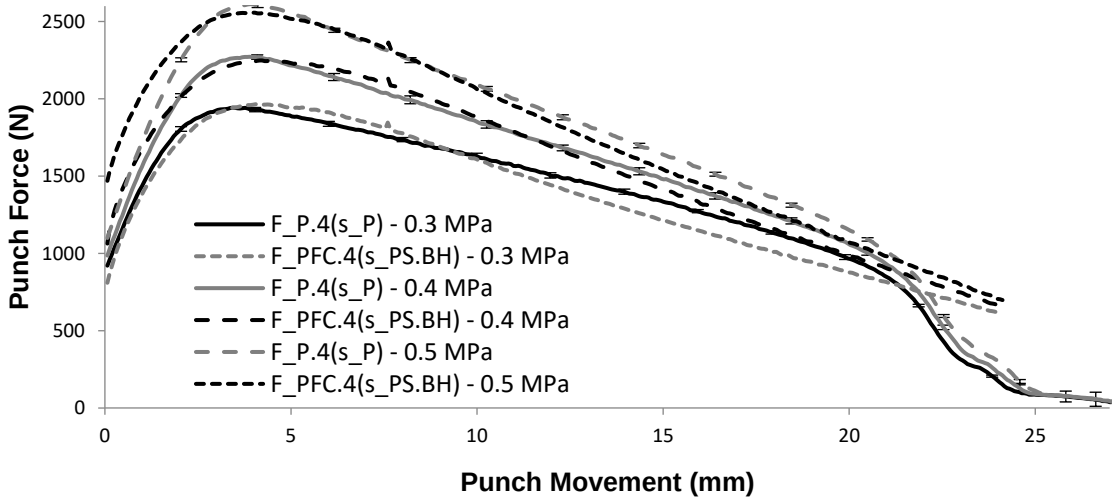

Fig. 21. Comparison between the adjusted punch force profile $F_{P.4}$ (s_P) and the empirical model of all active process force components $F_{PFC.4}$ ($s_{PS.BH}$) during forming process variant 4 for three blankholder pressure levels

CONCLUSIONS

1. The in-plane compression force can be measured without the disturbance of any friction force components within the newly developed in-plane compression testing method.
2. The in-plane compression force depends on the anisotropy of the paperboard sample material. In the main fiber direction, the resulting in-plane compression force was significantly higher than orthogonal to the main fiber direction. It was assumed that the resistance of the material structure depends only on the number of fibers aligned in the direction of the mechanical load.
3. The global maximum of the in-plane compression force was independent from the applied normal pressure. A higher normal pressure decreased only the out-of-plane tool displacement distance and therefore the free spaces where the excess material can go to avoid the in-plane compression force, probably resulting in a better distributed wrinkle formation.
4. With the IPCTM, samples can be produced with a distinctive wrinkle formation and characterized in subsequent substitute tests to evaluate their friction behavior and bending resistance. However, the dynamic coefficient of friction was independent of the wrinkle formation. On the other hand, the bending resistance increased for paperboard samples with a wrinkle formation in relation to paperboard samples without a wrinkle formation.
5. The triboelectric charging of uncoated paperboard material against unheated stainless steel tools at ambient temperature described in Lenske *et al.* (2017b, 2018), can be fully compensated by the application of self-adhesive PTFE-foil on the tool-sample surface. This significantly improved the reproducibility of the measurement data, which is why the number of individual tests within each test series can be significantly reduced. In addition to that, forming tools used within an industrial production line could be coated as well to prevent failures and enhance the production reliability.
6. The application of the PTFE-foil within the deep drawing process variants was only possible in the area below the blankholder. This created a height difference from the PTFE-foil to the stainless steel surface in the area of the infeed radius. This transition effect could be simulated with the DSTM and significantly reduced the dynamic coefficient of friction against the stainless steel surface. Because of that, the forming cavity could be coated only in the area below the blankholder, leaving the infeed radius and the inner contour of the forming cavity uncoated.
7. The comparison between the punch force profiles and the empirical model of all active punch force components during the validation strategy showed the eligibility of the newly developed method to investigate the in-plane compression behavior as a substitute test for the deep drawing process.

ACKNOWLEDGMENTS

The authors would like to thank Coesfeld Materialtest GmbH & Co. KG for technical support developing the friction tester and to Stefan Büttner, the Chair of Processing Machines and Mobile Machines of the TU Dresden, for software support.

REFERENCES CITED

Amontons, G. A. (1699). "De la resistance cause dans les machines [About resistance and force in machines]," *Memories de l´Academie Royale A* 275-282. DOI:

Bayer, R. G., and Sirico, J. L. (1971). "The friction characteristics of paper," *Wear* 17, 269-277. DOI: 10.1016/0043-1648(71)90030-5

Diaz, A. F., and Felix-Navarro, R. M. (2004). "A semi-quantitative tribo-electric series for polymeric materials: The influence of chemical structure and properties," *Journal of Electrostatics* 62(4), 277-290. DOI: 10.1016/j.elstat.2004.05.005

DIN 53121 (2008). "Testing of paper and board – determination of the bending stiffness by the beam method," German Institute for Standardization, Berlin, Germany.

DIN EN ISO 1924-2 (2009). "Paper and board – Determination of tensile properties – Part 2: Constant rate of elongation method (20 mm/s)," German Institute for Standardization, Berlin, Germany.

Dunitz, J. D., and Taylor, R. (1997). "Organic fluorine hardly ever accepts hydrogen bonds," *Chemistry – A European Journal* 3(1), 89-97. DOI: 10.1002/chem.19970030115

EN ISO 287 (2009). "Paper and board – Determination of moisture content of a lot – Oven drying method," European Committee for Standardization, Brussels, Belgium.

Galembeck, F., Burgo, T. A. L., Balestrin, L. B. d. S., Gouveia, R. F., Silva, C. A., and Galembeck, A. (2014). "Friction, tribochemistry and triboelectricity: Recent progress and perspectives," *Royal Society of Chemistry Advances* 4 (109), 64280-64298. DOI: 10.1039/c4ra09604e

Gurnagul, N., Ouchi, M. D., Dunlop-Jones, N., Sparkes, D. G., and Wearing, J. T. (1992). "Factors affecting the coefficient of friction of paper," *Journal of Applied Polymer Science* 46(5), 804-814. DOI: 10.1002/app.1992.070460508

Hauptmann, M. (2010). "Die gezielte Prozessführung und Möglichkeiten zur Prozessüberwachung beim mehrdimensionalen Umformen von Karton durch Ziehen [Process management and process monitoring during the deep drawing of paperboard]," *PhD Thesis, Technical University of Dresden*

Hauptmann, M., and Majschak, J. (2011). "New quality level of packaging components from paperboard through technology improvement in 3D forming," *Packaging Technology and Science* 24 (7), 419-432. DOI: 10.1002/pts.941

Hauptmann, M., Wallmeier, M., Erhard, K., Zelm, R., and Majschak, J. (2015). "The role of material composition, fiber properties and deformation mechanisms in the deep drawing of paperboard," *Cellulose* 22(5), 3377-3395.

Jeffrey, G. A. (1997). *An Introduction to Hydrogen Bonding*, Oxford Press, Oxford, UK.

Lenske, A., Müller, T., Hauptmann, M., and Majschak, J. (2018). "New method to evaluate the frictional behavior within the forming gap during the deep drawing process of paperboard," *BioResources* 13(3), 5580-5597. DOI: 10.15376/biores.13.3.5580-5597

Lenske, A., Hardtmann, A., Andrä, H. and Majschak, J.-P. (2017a). "Simulative und experimentelle Analyse des Umformvorgangs von Karton durch Ziehen [Simulative and experimental analysis of the deep drawing process of paperboard]," *Final report of research project IGF-18047BG* (www.ivlv.org)

Lenske, A., Müller, T., Penter, L., Schneider, M., Hauptmann, M., and Majschak, J. (2017b). "Evaluating the factors influencing the friction behavior of paperboard during the deep drawing process," *BioResources* 12(4), 8340-8358. DOI: 10.15376/biores.12.4.8340-8358

Mark, R. E. (2002). *Handbook of Physical Testing of Paper – Vol. 1*, Marcel Dekker Inc., New York, NY, USA.

Müller, T., Lenske, A., Hauptmann, M., and Majschak, J. (2017). "Method for fast quality evaluation of deep-drawn paperboard packaging components," *Packaging Technology and Science* 30(11), 703-710. DOI: 10.1002/pts.2315

Roudgar, A., and Gross, A. (2005). "Water bilayer on the Pd/Au(111) overlayer system: Coadsorption and electric field effects," *Chemical Physics Letters* 409(4-6),157-162. DOI: 10.1016/j.cplett.2005.04.103

Tabor, D. (1981). "Friction – The present state of our understanding," *Journal of Lubrication Technology* 103(2), 169-179. DOI: 10.1115/1.3251622

Wallmeier, M., Hauptmann, M., and Majschak, J. (2015). "New methods for quality analysis of deep-drawn packaging," *Packaging Technology and Science* 28(2), 91-100. DOI: 10.1002/pts.2091

Wallmeier, M., Barbier, C., Beckmann, F., Brandberg, A., Holqvist, C., Kulachenko, A. Moosmann, J., Östlund, S., Pettersson, T. (2021). "Phenomenological analysis of constrained in-plane compression of paperboard using micro-computed tomography Imaging," *Nordic Pulp & Paper Research Journal 36*(3), DOI: 10.1515/npprj-2020-0092

Zhang, Y., Pähtz, T., Liu, Y., Wang, X., Zhang, R., Shen, Y., Ji, R., and Cai, B. (2015). "Electric field and humidity trigger contact electrification," *Physical Review X* 5(1), article ID 011002. DOI: 10.1103/PhysRevX.5.011002

Article submitted: November 4, 2021; Peer review completed: January 8, 2022; Revised version received: February 14, 2022; Accepted: February 27, 2022; Published: March 6, 2022.
DOI: 10.15376/biores.17.2.2403-2427